RESEARCH ARTICLE

INTERNATIONAL RESEARCH JOURNAL OF MULTIDISCIPLINARY TECHNOVATION

Asian Research Association

DOI: 10.54392/irjmt24612

DFT Analysis on Adipic Acid to Propel Creative Advancements in Supercapacitor Technology

P. Divya [a, *]

[a] Department of Physics, Saveetha School of Engineering, Saveetha Institute of Medical and Technical Sciences (SIMATS), Thandalam, Chennai, India

* Corresponding Author Email: divyawelgen@gmail.com

DOI: https://doi.org/10.54392/irjmt24612

Received: 09-08-2024; Revised: 12-11-2024; Accepted: 18-11-2024; Published: 21-11-2024

Abstract: The increasing dependence on non-renewable resources for energy storage has accelerated the development of supercapacitor technology, which is now essential to portable devices and electric cars because of its high-power density and quick charge/discharge speed. Optimized geometry, weak C-H···O hydrogen bonding interactions inside methylene groups affect bond lengths, and the carboxylic group in adipic acid (ADPI) shortens bond lengths (C_{14}–C_{15} and C4–C_5). DFT simulations demonstrate a fair agreement to experimental data. According to vibrational studies, the O-H and C=O groups' vibrational frequencies are greatly influenced by the reactive hydrogen bonding displayed by the -COOH group in carboxylic acid derivatives. With theoretical values demonstrating significant PED contributions, these interactions reduce the O-H stretching frequency, which is seen as an O-H stretching band at 3405 cm^{-1} in the FT-IR spectra. In ADPI, atoms interact with neighboring atoms' σ* orbitals (O_2-C_4), (O_{12}-C_{14}), (C_4-C_5), (C_{14}-C_{15}), (O_1-C_4), and (O_{11}-C_{14}) through lone pairs of electrons localized on O_1 (LP^2), O_{11} (LP^2), O2 (LP1), and O_{12} (LP^1); these interactions have fairly high stabilization values of 33.78, 33.78, 17.91, 17.91, 6.75, and 6.75 kcal/mol, accordingly. Redox peaks and increased specific capacitance with scan rate are revealed by cyclic voltammetry study of ADPI, suggesting efficient electron transport, improved charge storage, and encouraging prospects for electrochemical energy storage applications. ADPI's appropriateness for high-performance electrochemical applications such as supercapacitors is supported by its impedance analysis, which is displayed by a Nyquist plot with a decreased semicircle and a sharp low-frequency slope. This plot demonstrates effective electron transfer, ion diffusion, and capacitive behavior.

Keywords: CV, Impedence, DFT, Adipic Acid, Non-Covalent, Supercapacitor Technology, FMO

1. Introduction

The need for new energy storage technologies that provide clean, renewable, and sustainable energy is expanding due to the depletion of non-renewable resources and the escalating pollution of the environment. Technological developments have prompted academics to look for alternatives to conventional energy storage systems in order to solve environmental problems resulting from the reliance on non-renewable resources. Supercapacitors are a very promising energy storage technology because of their extended lifespan, broad operating temperature range, quick charge/discharge rates, and outstanding power density. Supercapacitors, sometimes referred to as ultracapacitors, have drawn interest for their high-power density and quick charge-discharge capabilities in applications including electric cars and portable electronics. Depending on the materials utilized and the underlying energy storage process, supercapacitors are commonly divided into two types: electrochemical double-layer capacitors (EDLCs) and pseudocapacitors [1, 2]. While pseudocapacitors display reversible Faradic reactions, akin to those observed in rechargeable batteries, EDLCs store energy through non-faradic electrostatic interactions at the electrode/electrolyte interface. The physical and chemical characteristics of the electrode materials have a significant impact on supercapacitors' performance. The creation of effective electrode materials is essential to the advancement of supercapacitor technology. Because of their good electrical conductivity, high stability, huge surface area, and better power density, graphene-based materials are currently widely employed. However, their potential as supercapacitor electrode materials is limited by their comparatively poor energy density when compared to other storage devices [3, 4].

The choice of electrode materials significantly impacts the performance of supercapacitors. Researchers have explored various options, including carbon-based materials, metal-doped carbon

compounds, metal oxides, and hybrid metal oxide systems. The increasing demand for flexible supercapacitors in wearable and portable electronics has renewed interest in carbon-based substrates, such as carbon felt and carbon sheets, as potential electrode materials. Carbon felt, in particular, offers high electrical conductivity, excellent mechanical and thermal properties, cost-effectiveness, exceptional flexibility, and a large specific surface area (SSA) [5]. ADPI is an essential chemical compound with an annual production growth of 4%. It is used in the manufacture of fertilizers, lubricants, paper, waxes, and in the biomedical and food industries [6–8]. Traditional ADPI synthesis involves using HNO_3 with copper or vanadium catalysts, producing NOx by-products like N_2O_5 and N_2O, which negatively impact the environment [9]. To mitigate these issues, HNO_3-free methods employing H_2O_2, molecular oxygen, or microbial glucose conversion have been developed, although they face challenges such as safety concerns, longer reaction times, and lower yields [10]. This research focuses on the careful synthesis and characterization of ADPI using advanced techniques such as spectroscopy, density functional theory (DFT), and natural bond orbital (NBO) analysis, making this study unique. These methods provide a comprehensive understanding of the molecular structure and properties of ADPI, which is valuable for those interested in molecular design and materials science. Tools such as Gaussian'09 and Multiwfn exemplify the precision in computational analysis. By integrating studies on impedance and supercapacitance, this research paves the way for innovations in renewable energy integration and advancements in energy storage technology. Supercapacitors, also known as ultracapacitors, have become increasingly important as fast energy storage devices. They offer greater energy storage capacity than conventional capacitors, which has significantly expanded their applications over the past few decades [11–14]. Finally, the electrochemical performance of the newly synthesized compound as a supercapacitor was assessed using cyclic voltammetry (CV) and electrochemical impedance spectroscopy (EIS) techniques. The selection of electrode materials has a significant influence on the execution of supercapacitors. Numerous alternatives have been investigated by researchers, such as carbon-based supplies, metal-doped carbon compounds, metal oxides, and hybrid metal oxide systems. The growing need for flexible supercapacitors in wearable and portable electronics has led to a renewed interest in carbon-based substrates, such as carbon felt and carbon sheets, as possible electrode options. Among the numerous benefits of carbon felt are its high electrical conductivity, good mechanical and thermal qualities, affordability, and exceptional flexibility [15]. The careful characterisation of Adipic acid (ADPI) using cutting-edge methods like spectroscopy, DFT, & NBO analysis makes this study unique. These techniques offer in-depth understanding of the molecular structure and characteristics of ADPI for individuals interested in molecular design and materials science applications. Tools like Gaussian'09 and Multiwfn, which provide researchers with a dependable analytical framework, are prime examples of accuracy in computation. This research lays the door for new developments in renewable energy integration and creates avenues for advances in energy storage technologies by combining studies on impedance and supercapacitance[16].

2. Experimental Section Details

2.1 ADPI Crystal Growth

ADPI crystal was grown using analytical-grade precursors, which included equimolar quantities of adipic acid. To guarantee complete mixing, 0.9312 g of adipic acid (Loba Chemie) was dissolved in double-distilled water and constantly agitated for six hours at 20 °C using a temperature-controlled magnetic stirrer. To get a homogenous solution, continuous agitation was maintained throughout this period. To get rid of contaminants, the solution was filtered after being stirred. After allowing the solvent to evaporate, white, crystalline ADPI salt was produced. The crystals were allowed to dry naturally at room temperature. A number of recrystallization procedures were used to improve the crystals' purity and clarity. The saturated solution was allowed to gradually evaporate at room temperature in order to encourage the production of bulk ADPI crystals. High-quality ADPI crystals were formed after 30 days; Table 1 lists the specific features of these crystals, and Figure 1 shows the ORTEP diagram of ADPI.

2.2 Experimental Details

A variety of spectroscopic methods were used to characterize ADPI. Using the conventional KBr pellet approach, FT-IR spectra were collected on a Perkin Elmer spectrometer over a range of 4000–500 cm^{-1}. Using a UV-vis spectrophotometer, UV-visible absorption spectra in the 200–800 nm wavelength range were acquired. Electrochemical impedance spectroscopy (EIS) was used to analyze electrical parameters such as bulk ionic conductivity (σ). Using a 1.0 V AC signal, the impedance of a 0.009 cm-thick sample was measured between stainless steel electrodes by cutting it into 1 cm^2 squares. The tests were conducted between 42 Hz and 1 MHz.

3. Theoretical details

The Gaussian'09 program [17] was used to study the ADPI molecule computationally at B3LYP/6-311++G(d,p) level. Vibrational analysis was achieved utilizing the VEDA4 software [18] and PED interpretation. Molecular electrostatic potential (MEP) maps, which show the LUMO and HOMO states and are used to highlight regions of strong chemical activity,

were generated using Gauss View 5.0 [19]. The Multiwfn program [20] was utilized to conduct comprehensive wave function studies, which included electron localization function (ELF), RDG and localized orbital locator (LOL). The VMD software was utilized to generate isosurface visualizations [21].

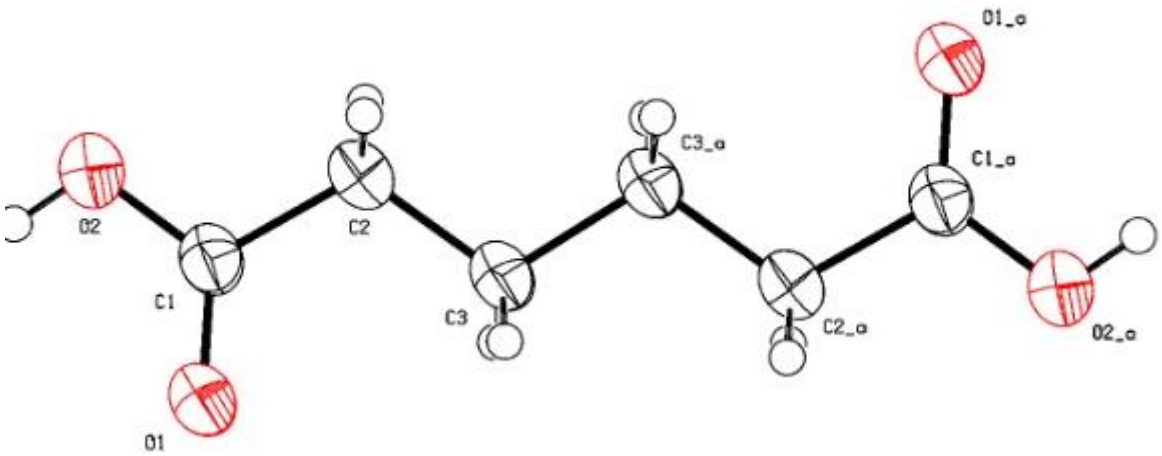

Figure 1. ORTEP diagram of adipic acid

Table 1. Crystal data and structure refinement for ADPI

Empirical formula	C6 H10 O4
Formula weight	146.14
Temperature	296(2) *K*
Wavelength	0.71073 *Å*
Crystal system, space group	Monoclinic, P 21/n
Unit cell dimensions	a = 7.3557(6) A alpha = 90 deg. b = 5.1483(4) A beta = 110.481(4) deg. c = 9.9955(9) A gamma = 90 deg.
Volume	354.60(5) A^3
Z, Calculated density	*2, 1.369 Mg/m³*
Absorption coefficient	*0.116 mm⁻¹*
F(000)	156
Crystal size	*0.250 x 0.250 x 0.200 mm*
Limiting indices	-9<=h<=9, -5<=k<=6, -13<=l<=13
Reflections collected / unique	11402 / 4603 [R(int) = 0.0276]
Theta range for data collection	2.995 to 28.360 deg.
Completeness to theta = 25.242	100.0 %
Max. and min. transmission	0.977 and 0.972
Refinement method	Full-matrix least-squares on F^2
Data / restraints / parameters	854 / 0 / 48
Goodness-of-fit on F^2	1.050
Final R indices [I>2sigma(I)]	R1 = 0.0442, wR2 = 0.1240
R indices (all data)	R1 = 0.0515, wR2 = 0.1348
Extinction coefficient	1.17(10)
Largest diff. peak and hole	0.215 and -0.202 $e.A^{-3}$

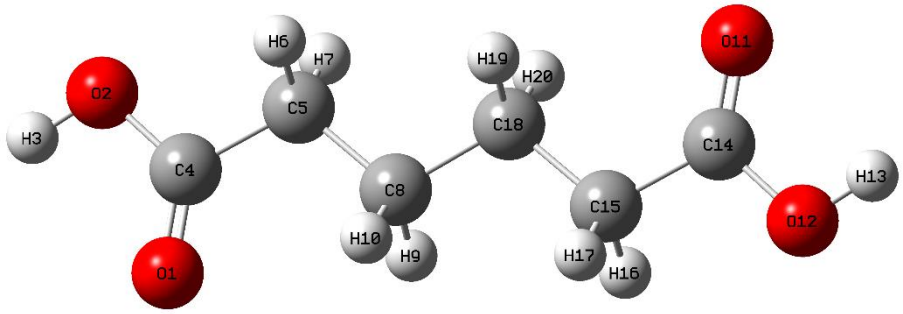

Figure 2. **Optimized structure of adipic acid molecule for gas phase.**

Table 2. **Optimized Bond lengths (*Å*) and bond angles (°) by B3LYP/6-311G(d,p) with XRD data of ADPI**

Bond length	DFT	EXP	Bond angle	DFT	EXP
O_1-C_4	1.2054	1.2213	H_3-O_2-C_4	107.2	109.5
O_2-H_3	0.9691	0.82	O_1-C_4-O_2	122.3	122.9
O_2-C_4	1.3581	1.2944	O_1-C_4-C_5	126.4	122.9
C_4-C_5	1.5103	1.4934	O_2-C_4-C_5	112.3	114.2
C_5-H_6	1.0959	0.97	C_4-C_5-H_6	107.5	108.6
C_5-H_7	1.0959	0.97	C_4-C_5-H_7	107.5	108.6
C_5-C_8	1.5281	1.5069	C_4-C_5-C_8	113.6	114.8
C_8-H_9	1.0948	0.9701	H_6-C_5-H_7	105.3	107.5
C_8-H_{10}	1.0948	0.9701	H_6-C_5-C_8	111.3	108.6
C_8-C_{18}	1.5319	1.515	H_7-C_5-C_8	111.3	108.6
O_{11}-C_{14}	1.2054	1.2213	C_5-C_8-H_9	109.2	109.1
O_{12}-H_{13}	0.9691	0.82	C_5-C_8-H_{10}	109.2	109.1
O_{12}-C_{14}	1.3581	1.2944	C_5-C_8-C_{18}	112.2	112.4
C_{14}-C_{15}	1.5103	1.4934	H_9-C_8-H_{10}	105.9	107.9
C_{15}-H_{16}	1.0959	0.97	H_9-C_8-C_{18}	110.1	109.1
C_{15}-H_{17}	1.0959	0.97	H_{10}-C_8-C_{18}	110.1	109.1
C_{15}-C_{18}	1.5281	1.5068	H_{13}-O_{12}-C_{14}	107.2	109.5
C_{18}-H_{19}	1.0948	0.9701	O_{11}-C_{14}-O_{12}	122.3	122.9
C_{18}-H_{20}	1.0948	0.9701	O_{11}-C_{14}-C_{15}	126.4	122.9
			O_{12}-C_{14}-C_{15}	111.3	114.2
			C_{14}-C_{15}-H_{16}	107.5	108.6
			C_{14}-C_{15}-H_{17}	107.5	108.6
			C_{14}-C_{15}-C_{18}	113.6	114.8
			H_{16}-C_{15}-H_{17}	105.3	107.5
			H_{16}-C_{15}-C_{18}	111.3	108.6
			H_{17}-C_{15}-C_{18}	111.3	108.6
			C_8-C_{18}-C_{15}	112.2	112.4
			C_8-C_{18}-H_{19}	110.1	109.1
			C_8-C_{18}-H_{20}	110.1	109.1
			C_{15}-C_{18}-H_{19}	109.2	109.1
			C_{15}-C_{18}-H_{20}	109.2	109.1
			H_{19}-C_{18}-H_{20}	105.9	107.9

4. Results and Discussion

4.1 Conformation Studies

4.1.1 Optimisation Studies

ADPI's molecular makeup is symmetrical in the C1 point group. In the gas phase, it is discovered that the lowest SCF energy of ADPI is -535.606 a.u. Figure 2 shows the ADPI's optimized shape with atom numbering. Utilizing the above said basis set, the DFT technique was used to examine standardized structural variables, which are displayed in Table 2 as bond lengths (BL) and bond angles (BA). A correlation analysis was conducted among the geometric attributes of the basis set (B3LYP/6–311++G(d,p)) calculated and experimental. The computed RMSD values for the relevant actual bond lengths (BL) & bond angles (BA) in comparison to the optimal ones were 0.98997 (BL) & 0.94269 (BA). These RMSD values are near one, indicating that the actual and theoretical bond properties coincide perfectly.

The carboxylic group shortens the bond lengths C_{14}-C_{15} and C_4-C_5 compared to the methylene groups linked via the C_8-C_{18} bond, with actual and DFT values of 1.5319 Å and 1.5069 Å, respectively. In ADPI, bond lengths inside methylene groups (1.0948 - 1.0959 Å) are diminished due to weak C-H···O hydrogen bonding interactions that are smaller than the vdW gap. The bond angles (O_2-C_4-C_5) and (O_1-C_4-O_2) were estimated theoretically to be 122.3° and 112.3°, respectively, which is in close agreement with the stated values of 122.9° and 114.2°. The computed C–C–C angles in ADPI showed good agreement with known values spanning 112.2° to 113.6°, falling between 112.4° and 114.8°. Because of its large electronegative charge, oxygen aggressively tries to pull electrons from neighboring atoms and move them closer together for simpler electron sharing. The experimental bounds for the BA of C–C–H & H–C–H were 105.5°–107.5° and 107.5°–108.6°, respectively. It is possible to ascribe the 3.5° discrepancy between the estimated bond angle of O_1-C_4-C_5 (126.4°) and the observed angle (122.9°) to the existence of the electronegative oxygen atom (O_1) inside the carboxylic group. With its increased ability to extract electrons, this oxygen atom may impact the electron density surrounding the hydrogen & carbon atoms. This can result in a somewhat reduced bond angle relative to the anticipated value, characterizing the molecule's electrical interactions. In contrast to the stated experimental result of 109.5°, the bond angle of (C–OH) was determined to be 107.2°. Theoretically, bond angles for O-C-C were simulated within the 111.3°–126.4° range. The recorded range for the matching experimental values was 114.2° - 122.9°

4.1.2 Vibrational assignments

ADPI is made up of 20 atoms in its molecular structure, each of which can vibrate in 54 different ways. Using the B3LYP/6-311++G(d,p) basis set and the DFT approach, the initial vibrational wavelengths of ADPI were discovered, as indicated in Table 3. Figure 4 displays the FT-IR spectrum of ADPI that was obtained computationally and practically. To account for the mistakes caused by ignoring anharmonicity effects, the calculated frequencies of vibration were scaled by 0.961. The matching association graph between the ADPI 's experimental and theoretical FT-IR wavenumbers is displayed in Figure 3.

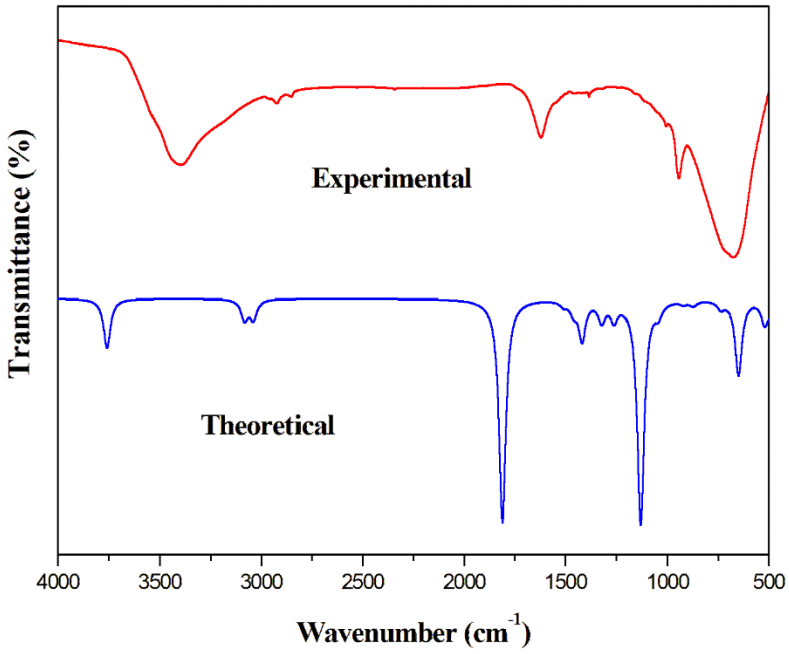

Figure 3. Experimental and Simulated FT-IR spectra

Table 3. Calculated vibrational frequencies of adipic acid by B3LYP/6-311++G(d, p) basis set.

Modes	Unscaled	Scaled	FT-IR	Assignments (PED%)
1	3758.73	3612		vOH (100)
2	3758.62	3612	3405	vOH (100)
3	3083.04	2963	2965	ν_{AS}CH (12)+ν_{AS}CH (17)+ν_{AS}CH (63)
4	3066.76	2947		ν_{SS}CH (80)+ν_{AS}CH (15)
5	3053.14	2934		ν_{SS}CH (69)+ν_{AS}CH (18)
6	3045.51	2927	2926	ν_{SS}CH (80)+ν_{AS}CH (11)
7	3040.58	2922		ν_{AS}CH (15)+vCH (14)+vCH (61)
8	3032.66	2914		ν_{SS}CH (81)+ν_{SS}CH (13)
9	3027.78	2910		ν_{AS}CH (13)+ν_{SS}CH (81)
10	3026.52	2908	2854	ν_{SS}CH (73)+ν_{AS}CH (17)
11	1812.26	1742		vOC (84)
12	1811.21	1741	1625	vOC (84)
13	1508.1	1449		βHCH (94)
14	1491.46	1433		βHCH (94)
15	1462.95	1406		βHCH (84)
16	1459.73	1403		βHCH (84)
17	1423.05	1368	1388	τHCCC (46)
18	1418.35	1363		vCC (14)+τHCCO (48)
19	1374.68	1321		vCC (19)+βHOC (10)+τHCCC (41)
20	1332.49	1281		βHCC (63)+βHCC (10)+τHCCC (11)
21	1329.21	1277		βHCC (67)+βHCC (11)
22	1321.61	1270		vOC (12)+βHOC (38)+βCCO (13)+τHCCC (13)
23	1292.71	1242		βHOC (52)+τHCCC (18)
24	1271.84	1222		βHCC (64)
25	1261.06	1212		βHOC (24)+τHCCC (48)
26	1168.86	1123		βHCC (15)+βHCC (57)
27	1155.52	1110		vCC (41)+βHOC (19)
28	1131.92	1088		vOC (51)+βHOC (21)
29	1107.95	1065		τHCCC (45)+τHCCC (18)
30	1086.01	1044		vCC (59)+βCCC (12)
31	1048.12	1007	1006	vCC (63)
32	1045.21	1004	947	vCC (80)
33	920.5	885		τHCCC (11)+τHCCO (45)
34	888.26	854		vOC (71)
35	872.66	839		vCC (52)+βCCO (12)
36	804.81	773		τHOCC (13)+τHCCC (17)+τHOCC (14)
37	736.69	708	677	βHCC (20)+τHCCC (15)+τHCCO (39)
38	649.86	625		τHOCC (80)
39	648.67	623		vOC (15)+βCCO (65)
40	647.15	622		τHOCC (74)
41	625.17	601		vCC (13)+βOCO (68)
42	520.61	500		τHOCC (74)
43	517.99	498		τCCCO (11)+τHOCC (61)
44	504.54	485		βCCC (10)+βCCO (79)
45	474.25	456		vCC (13)+βCCO (69)

46	329.18	316		βCCC (86)
47	255.27	245		vOC (14)+vCC (21)+βCCC (50)
48	171.08	164		βCCC (14)+βCCC (66)
49	131.62	126		τHCCO (14)+τHCCC (12)+τCCCC (59)
50	117.91	113		τCCCC (85)
51	74.25	71		βCCC (94)
52	50.44	48		τHCCC (13)+τCCCO (62)
53	46	44		τCCCC (87)
54	21.72	21		τCCCC (79)

d: v- stretching, β- bending, ω- wagging, τ- torsion

4.1.2.1 COOH vibrations

The -COOH group is reactive and participates in hydrogen bonding networks, making vibrational investigations into this group essential. As a result, while investigating -COOH derivatives, the vibrations of the -OH and C=O groups are important indications. H-bonded entity spectra show that the vibrations of the hydroxyl groups are very sensitive to changes in their surroundings. The vibrational band usually emerges between 3700 and 3584 cm^{-1} in hydrogen-bonded -OH groups [22]. The strong polarization of the carboxylic acid position allows hydrogen bonds to develop with solvents such as alcohols and water, as well as with other polar substances. Alteration in the surroundings has a significant impact on the O-H group vibrations, resulting in the hydrogen bonding spectra into reduced frequency sections of elevated intensity. The crystallized makeup of the molecule forms H-bond interactions, which are responsible for this behavior. An O-H stretching band was detected in the FT-IR spectrum of the current investigation at 3405 cm^{-1}. A matching estimated value of 3612 cm^{-1}, yielding 100% to PED, indicated thorough stretching. The development of non-covalent contacts, namely C-H-O hydrogen bonds, explains the frequency shift downward of the vOH vibration. The bending HOC mode corresponds to theoretical bands at 1242 and 1212 cm^{-1} in the scaled spectra. The impact of HB interactions brought on by the carboxylic group's existence is responsible for the enhanced values of O-H in-plane bending vibrations. A partial charge is placed on the oxygen atom receiving the hydrogen bond as well as the atom supplying the hydrogen when a carbonyl group engages in hydrogen bonding, which might result in resonance. This resonance effect increases the C=O stretching wavenumber, which is reduced owing to the proton's partial "transfer of allegiance". The carbonyl stretching mode is lowered in the crystal when the carbonyl group chelates in alongside additional nucleophilic groups to establish intra- and intermolecular hydrogen ties. There is a good match between the scaled value of 1741 cm^{-1} and faintest band in the IR at 1625 cm^{-1}.

4.1.2.2 CH_2 Vibrations

The region of 3100–2950 cm^{-1} is vas CH_2 groups are usually observed, whereas vss appear around 2900–2800 cm^{-1} [23]. One notable difference between aromatic ring stretching (C-H) vibrations and CH2 stretching vibrations is their frequency. Mild to moderate bands at 2965, 2926, and 2854 cm^{-1} in the FT-IR resemble to symmetric and asymmetric CH_2 stretching in ADPI. The vibrations at 2963, 2947, 2934, 2927, 2922, 2914, 2910, and 2908 cm^{-1} have matching computed wavenumbers that show excellent PED values. Intramolecular C-H···O hydrogen bonding contacts are responsible for the change in wavenumber for the s vss CH_2 from the predicted range.

4.2 Transition Studies

4.2.1 NBO Analysis

A helpful framework for analyzing the high ED in molecular systems' orbital bonding is provided by NBO research [24]. Using second-order perturbation theory with the Fock matrix in the NBO basis, NBO analysis was carried out in the case of ADPI to assess electron-occupied orbitals and unoccupied orbitals). The amount of conjugation within the system and the donor-acceptor relationships are better understood owing to this investigation. The header composite underwent an NBO analysis at the above said level. Table 4 summarizes electron supplier and receiver orbitals and provides the stabilization energies (E(2)) for important intramolecular CT contacts. A key factor in keeping the combination stable is the interactions between oxygen atoms' lone pair orbitals. In ADPI, atoms interact with neighboring atoms' σ* orbitals (O_2-C_4), (O_{12}-C_{14}), (C_4-C_5), (C_{14}-C_{15}), (O_1-C_4), and (O_{11}-C_{14}) through lone pairs of electrons localized on O_1 (LP^2), O_{11} (LP^2), O2 (LP1), and O_{12} (LP^1); these interactions have fairly high stabilization values of 33.78, 33.78, 17.91, 17.91, 6.75, and 6.75 kcal/mol, accordingly because -COOH and -OH groups that are joined to the ring have the ability to donate and take electrons, which increases the resonance inside the ring. The C=O bond contracts as a result of this interaction, which is fueled by the bonding orbital contacts with the oxygen atom and amply demonstrates the ring's

enhanced resonance. The NBO analysis revealed a significant intramolecular charge transfer from σ orbitals [(O_2-H_3), (O_{12}-H_{13}), (C_8-H_9), (C_8-H_{10}), (C_{18}-H_{19}), (C_{18}-H_{20}), (C_8-H_9), (C_8-H_{10})] to σ* orbitals [(C_4-C_5), (C_{14}-C_{15}), (C_5-H_6), (C_5-H_7), (C_{15}-H_{16}), (C_{15}-H_{17}), (C_{18}-H_{19}), (C_{18}-H_{20})], with stabilization energies fluctuating between 3.55 to 2.78 kcal/mol.

4.2.2 FMO study

Essential evidence on the electrical and optical characteristics of molecules can be obtained by utilizing FMOs, particularly LUMO and the HOMO [25]. These orbitals are essential for comprehending quantum chemical characteristics and UV-Vis spectra, as well as for elucidating a variety of conjugated system processes [26]. According to the FMO concept, the reactive ability of compounds is related to molecular orbital energies and orbital coefficients; in particular, HOMO and LUMO are crucial since they denote the outer limits of electron possession in a system.

Table 4. Second order perturbation theory analysis of Fock matrix in NBO basis

Type	Donar (i)	ED (i) (e)	Type	Acceptor (j)	ED (j) (e)	E (2)[a] kcal/mol
$LP^{(2)}$	O_2	1.83052	π*	O_1 - C_4	0.20483	43.4
$LP^{(2)}$	O_{12}	1.83052	π*	O_{11} - C_{14}	0.20483	43.4
$LP^{(2)}$	O_1	1.85025	σ*	O_2 - C_4	0.09990	33.78
$LP^{(2)}$	O_{11}	1.85025	σ*	O_{12} - C_{14}	0.09990	33.78
$LP^{(2)}$	O_1	1.85025	σ*	C_4 - C_5	0.06011	17.91
$LP^{(2)}$	O_{11}	1.85025	σ*	C_{14} - C_{15}	0.06011	17.91
$LP^{(1)}$	O_2	1.97764	σ*	O_1 - C_4	0.02199	6.75
$LP^{(1)}$	O_{12}	1.97764	σ*	O_{11} - C_{14}	0.02199	6.75
σ	O_2 - H_3	1.98701	σ*	C_4 - C_5	0.06011	3.55
σ	O_{12} - H_{13}	1.98701	σ*	C_{14} - C_{15}	0.06011	3.55
σ	C_8 - H_9	1.97887	σ*	C_5 - H_6	0.01344	2.96
σ	C_8 - H_{10}	1.97888	σ*	C_5 - H_7	0.01344	2.96
σ	C_{18} - H_{19}	1.97887	σ*	C_{15} - H_{16}	0.01344	2.96
σ	C_{18} - H_{20}	1.97888	σ*	C_{15} - H_{17}	0.01344	2.96
σ	C_8 - H_9	1.97887	σ*	C_{18} - H_{19}	0.01540	2.78
σ	C_8 - H_{10}	1.97888	σ*	C_{18} - H_{20}	0.01540	2.78
σ	C_5 - H_6	1.96447	σ*	C_8 - H_9	0.01540	2.6
σ	C_5 - H_7	1.96446	σ*	C_8 - H_{10}	0.01540	2.6
σ	C_{15} - H_{16}	1.96447	σ*	C_{18} - H_{19}	0.01540	2.6
σ	C_{15} - H_{17}	1.96445	σ*	C_{18} - H_{20}	0.01540	2.6
σ	C_5 - H_6	1.96447	σ*	O_1 - C_4	0.02199	2.45
σ	C_5 - H_7	1.96446	σ*	O_1 - C_4	0.02199	2.45
σ	C_{15} - H_{16}	1.96447	σ*	O_{11} - C_{14}	0.02199	2.45
σ	C_{15} - H_{17}	1.96445	σ*	O_{11} - C_{14}	0.02199	2.45
$LP^{(1)}$	O_1	1.97829	σ*	C_4 - C_5	0.06011	2.4

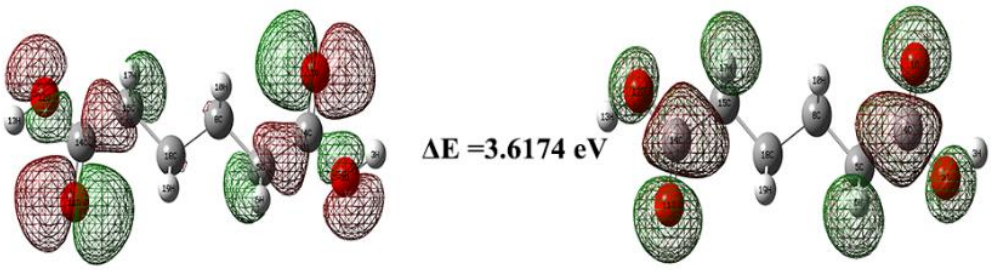

Figure 4. Frontier molecular orbitals of adipic acid

Table 5. Calculated energy values of title compound by B3LYP /6-311++G(d, p)

Parameters (eV)	Gas
E_{HOMO}	-5.477
E_{LUMO}	-1.859
Energy band gap (ΔE)	3.6174
Ionization potential	5.4773
Electron affinity	1.8599
Chemical hardness	1.809
Chemical Softness	0.276
Electro negativity	3.669
Chemical potential	-3.669
Electrophilicity index	3.721
Electron donating capability (ω^-)	5.781
Electron accepting capability (ω^+)	2.112
Net electrophilicity ($\omega^{\pm}$)	7.893
Nucleophilicity index (N)	0.269

Table 6. Experimental and theoretical UV–vis Characteristics of adipic acid molecule in DMSO

No.	Experimental	Energy (cm-1)	Wavelength (nm)	Oscillatory Strength	Symmetry	Major contribs
1		47872.56	208.9	0.0005	Singlet-A	H-1->L+1 (48%), HOMO->LUMO (49%)
2		47874.98	208.8	0	Singlet-A	H-1->LUMO (48%), HOMO->L+1 (49%)
3	178	56673.74	176.4	0.1213	Singlet-A	H-1->L+2 (62%), HOMO->L+3 (35%)

Employing the B3LYP/6-311++G(d,p) basis set, the HOMO and LUMO orbital visual representations for ADPI were computed, as illustrated in Figure 4. In ADPI the ionization potential (I) and the HOMO, which represents the molecule's electron-donating (nucleophile) capacity, are proportional. In contrast, the LUMO energy is precisely associated to electron affinity (A) and indicates the molecule's propensity for accepting an electron (electrophile) [27]. With computed energies of EHOMO = -5.477 eV & ELUMO = -1.859 eV, the HOMO & LUMO are both concentrated over the carboxylic acid group, as shown in Fig. 5. The energy gap that results, which is 3.6174 eV, describes the CT contacts within the complex and shows the chemical strength of ADPI. To further elucidate these qualities, Table 5 presents the global reactivity parameters that have been determined. Organic compounds are characterized as being robust electrophiles (ω > 1.5 eV), medium electrophiles (0.8 < ω < 1.5 eV), or feeble electrophiles (ω < 0.8 eV) according to the electrophilicity index (ω)[28]. Considering its greater ω value, ADPI appears to be a potent electrophile.

4.2.3 UV Study

The UV-visible spectrum for ADPI in DMSO solvent was determined utilizing the TD-DFT technique [29, 30], as Figure 5 illustrates. Table 6 shows the chemical orbital contributions, wavelengths, energy band gaps, and absorption energy. ADPI in DMSO

showed a broad absorbance spectrum at 186 nm, which corresponds to a π-π* transition. The wavelengths at which the data could be obtained were 208.9, 208.8, and 182.4 nm. The observed absorbance peaks match electron transitions between border orbitals, namely from HOMO to LUMO, according to computational models. According to the estimated absorption spectra, the maximum absorption wavelength is associated with electronic shifts from H-1 -> L+2 (62%) and HOMO -> L+3 (35%).

4.3 Non-Covalent Interaction Analysis

4.3.1 ELF and LOL Analysis

The ELF & LOL are important tools for surface and topological investigation in molecular systems. LOL (r) and ELF τ(r) form the essential basis of the electron localization that the Lewis structure describes [31,32]. These functions provide the foundation for comprehending the distribution of electron pairs in molecular space; the gradients of orbitals give birth to maximum localized orbital overlap, which is signified by LOL and electron pair density by ELF [33].

The wave analysis tool Multiwfn was used to analyze electrical wave functions and create mapping graphics of ELF and LOL [34]. The color-shaded patterns of LOL and ELF are shown in Figure 6. On the ELF map, values are represented by a color scale from blue to red, whereas on the LOL map, values are represented by a scale from 0.5 to 1.0. The regions of bonding and nonbonding localized electron density are highlighted in both maps by a span from 0.5 to 1.0, whereas delocalized electron zones are highlighted by values below 0.5 [35]. The LOL maps show that the highest values are obtained at scales above 0.5 in regions where ED drives electron localization. The existence of bonding & nonbonding electrons is verified by the color variations in the LOL & ELF visualizations. Regarding the hydrogen atoms (H_{16}, H_{17}, H_{19}, H_{20}, H_9, H_{10}, H_6, H_7), the color red denotes areas exhibiting elevated bonding and nonbonding electron localization values. In Figure 6, on the other hand, low electron localization values are indicated by the blue coloring surrounding carbon atoms. Little blue circles surrounding carbon atoms (C_{15}, C_{18}, C_8, C_5) indicate electron depletion throughout the valence and inner shell. As seen in Figure 6, minimal white circles surrounding hydrogen atoms with elevated LOL values represent regions of maximal electron density [36], whereas the red color near these hydrogen atoms indicates covalent connections between the atoms.

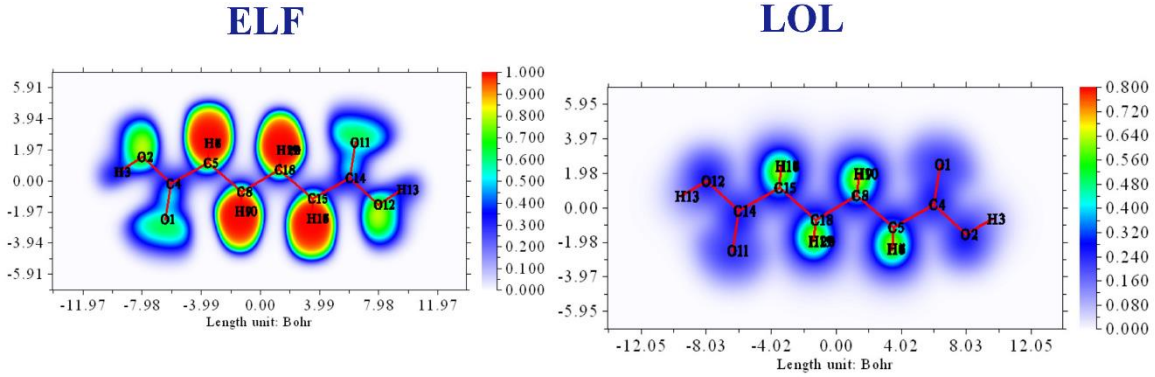

Figure 6. Electron localization function (ELF) map and Localized orbital locator (LOL) maps in the gas phase

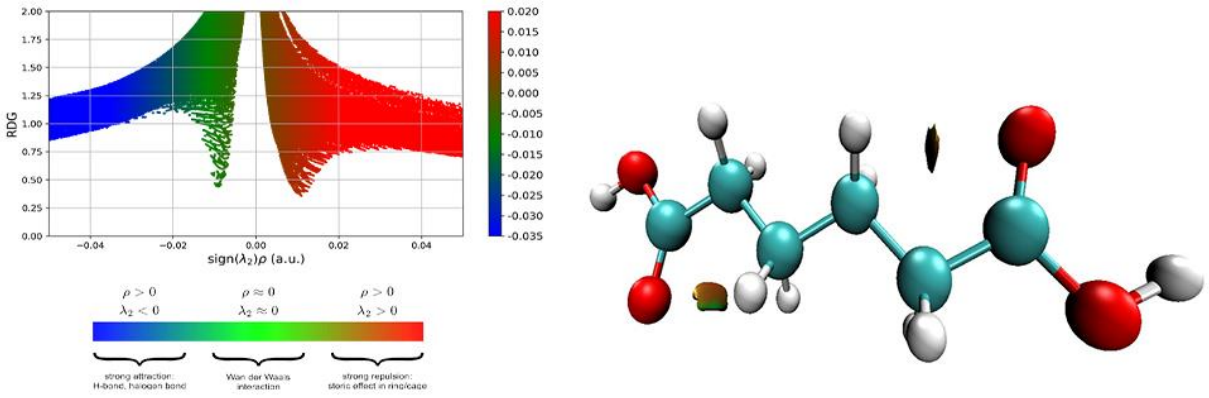

Figure 7. 2D scatter and Isosurface density plots illustrating the non-bonded interactions of adipic acid

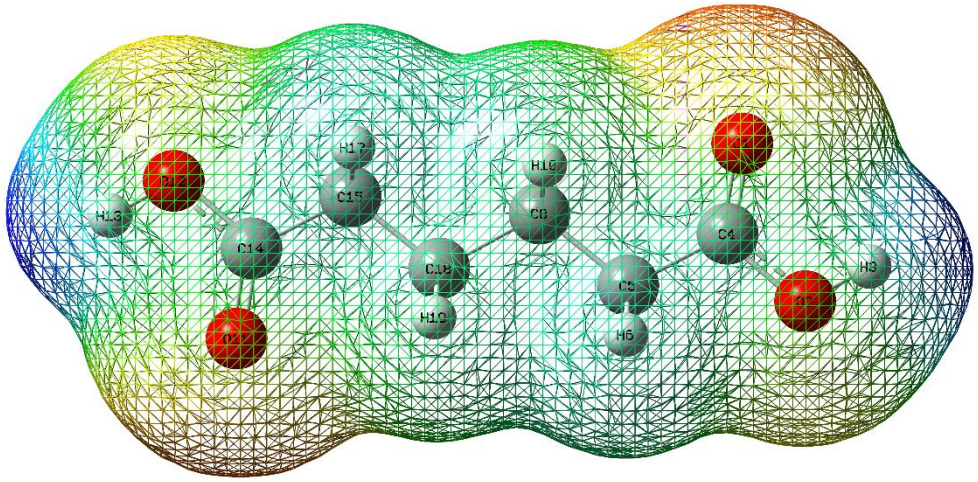

Figure 8. MEP map for adipic acid

4.3.2 RDG Studies

Analyzing noncovalent interactions (NCIs) or Reduced Density Gradients (RDGs) in molecular systems is a great way to learn about weak connections[37]. This method visualizes these interactions by using the RDG's isosurface[38]. Electron density is the basis for accurate estimation of weak relationships in real space; a low-density gradient represents regions of weakened connections, while a high-density gradient emphasizes regions of substantial interaction[39]. In the investigation of NCI in ADPI, a visual examination of weak links was conducted using the RDG technique and Atomistica [40,41]& VMD software. A coloured scatter map (graph) produced by the Multiwfn tool with an isovalue of 0.5 is shown with the NCI in ADPI in Figures 7. The lack of a ring structure is probably the reason for the results, which show no steric impacts. It is found that hydrogen bonding occurs when a hydrogen atom forms a bridge among two electronegative atoms, one via a covalent connection and the other by an electrostatic attraction. Mixed flaky patches in green and red show the presence of moderate noncovalent relationships such as C-H···O. The RDG chart, which displays values spanning 0.01 to -0.02 a.u., provides more evidence for these relationships.

4.4 Charge Analysis

4.4.1 MEP Studies

Protons' interactions with electrons and neutrons through a molecule's electric charge cloud are depicted visually in MEP maps. A 3D representation of the electrostatic potential inside a molecule is provided by these maps, which are sometimes referred to as MEP surfaces [42,43]. 3D color-coded MEP images with a scaling range were produced in this study using the GaussView 5.0 [19] program. Red indicates areas of strongest attraction, whereas blue indicates areas of greatest repulsion on the MEP maps, which are color-coded in red, yellow, green, and blue. In Figure 8, the 3D MEP picture is displayed. Finding reactive locations within the molecule and determining the compound's physicochemical connection are made possible by MEP analysis [44]. The MEP chart's scaling range is -6.183 × 10^{-2} (red), which represents the greatest enticement, to 6.183 × 10^{-2} (blue), which represents the strongest repelling. The illustration shows that the carbonyl group's oxygen atoms display a positive prospective cloud. The green hue, which emphasizes the methylene categories in ADPI, represents the neutral potential. Moreover, the positive potential across the hydroxyl group is represented by the color blue on the diagram.

4.5 CV Analysis

In a cyclic voltammetry (CV) analysis, ADPI demonstrates redox behavior characterized by oxidation and reduction peaks in the CV graph, indicating its capability for electron transfer. The specific capacitance values calculated for ADPI at different scan rates are 11.77 F/g at 10 mV/s, 17.69 F/g at 20 mV/s, 33.35 F/g at 30 mV/s, 37.26 F/g at 40 mV/s, 38.88 F/g at 50 mV/s, 40.06 F/g at 60 mV/s, 50.11 F/g at 80 mV/s, 50.99 F/g at 100 mV/s, and 73.80 F/g at 200 mV/s (figure 9). These values show that as the scan rate increases, the specific capacitance also increases, suggesting more efficient charge storage and faster ion diffusion at higher scan rates, likely due to improved accessibility of active sites on the electrode, which is crucial for ADPI's potential application in electrochemical energy storage devices. The supercapacitor system's maximum charge storage capacity efficiency was demonstrated at a scan rate of 200 mV/s. Specific capacitance is influenced by a number of variables, including scan rate, electrode surface area, and material properties; therefore, it is important to optimize scan rate in order to increase

capacitance. The promise of ADPI for energy storage applications may be highlighted by additional research into the underlying mechanisms and material properties, which could yield important insights for creating high-performance supercapacitors.

4.7 Impedance Analysis

ADPI's impedance study usually shows a semicircle at high frequencies and a linear region at low frequencies, which represent the material's ion diffusion and charge transfer resistance, respectively. The real and imaginary components of impedance at different frequencies are displayed for ADPI in the data provided, which are used to explain its electrochemical activity. Effective electron transfer at the electrode-electrolyte interface is shown by a reduced diameter of the semicircle in the Nyquist plot (figure 10), which also shows a lower charge transfer resistance. Ion diffusion through the electrolyte is indicated by the low-frequency linear part, which is frequently connected to the Warburg impedance. Better capacitive behavior is indicated by a steeper slope in the low-frequency zone, but lower impedance values at high frequencies suggest better conductivity. Understanding these properties is essential to comprehending the effectiveness of ADPI in electrochemical systems, especially in applications like supercapacitors where high capacitance and low impedance are required for quick charge-discharge cycles.

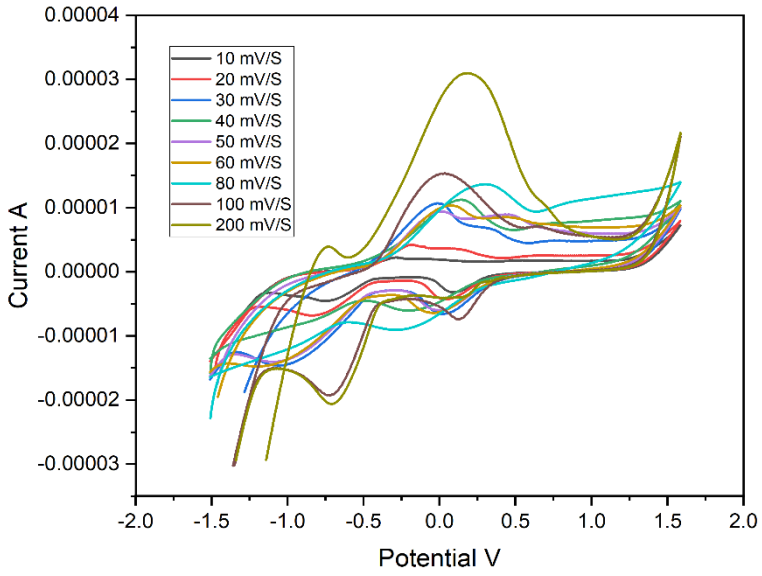

Figure 9. **Cyclic volumetric analysis of adipic acid at various scan rates**

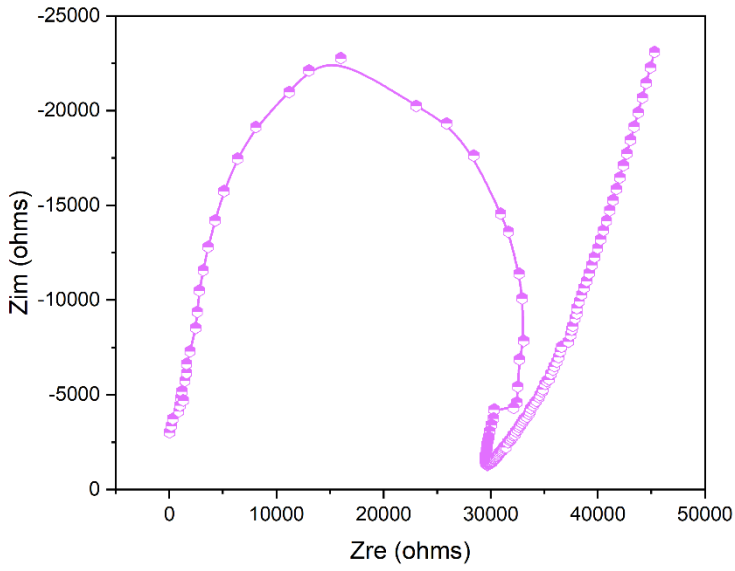

Figure 10. **Nyquist plot of adipic acid**

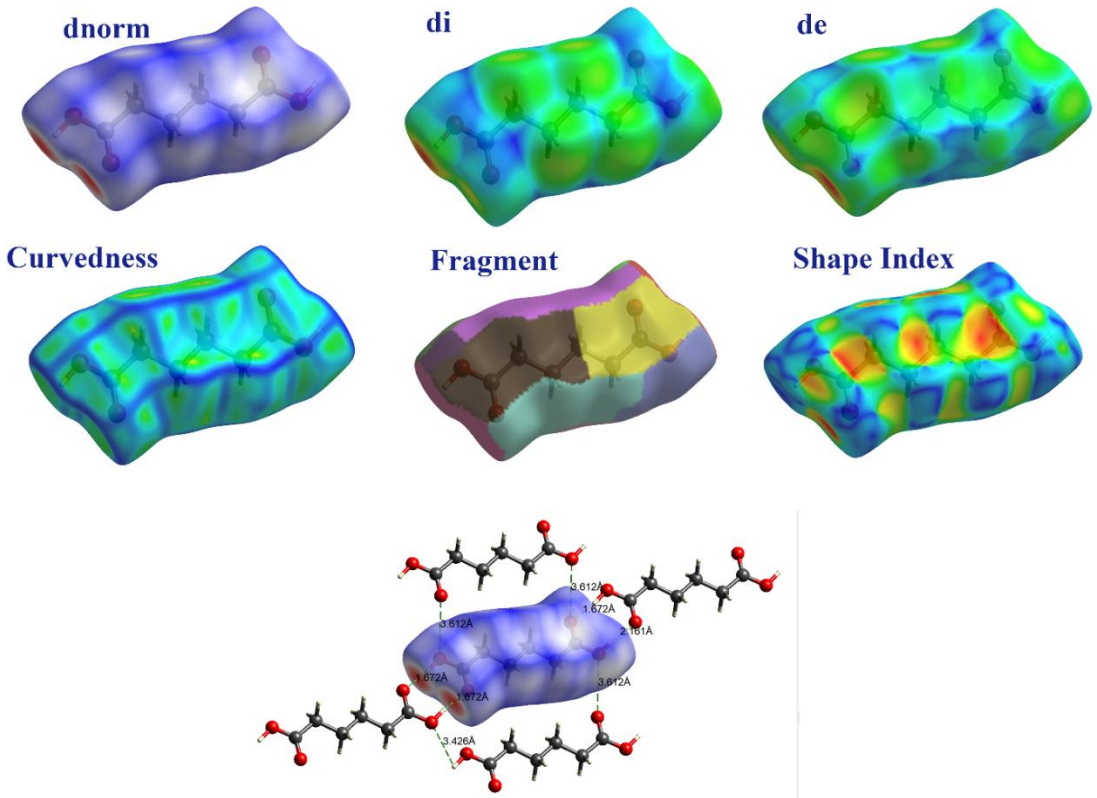

Figure 11. Hirshfeld surfaces of adipic acid

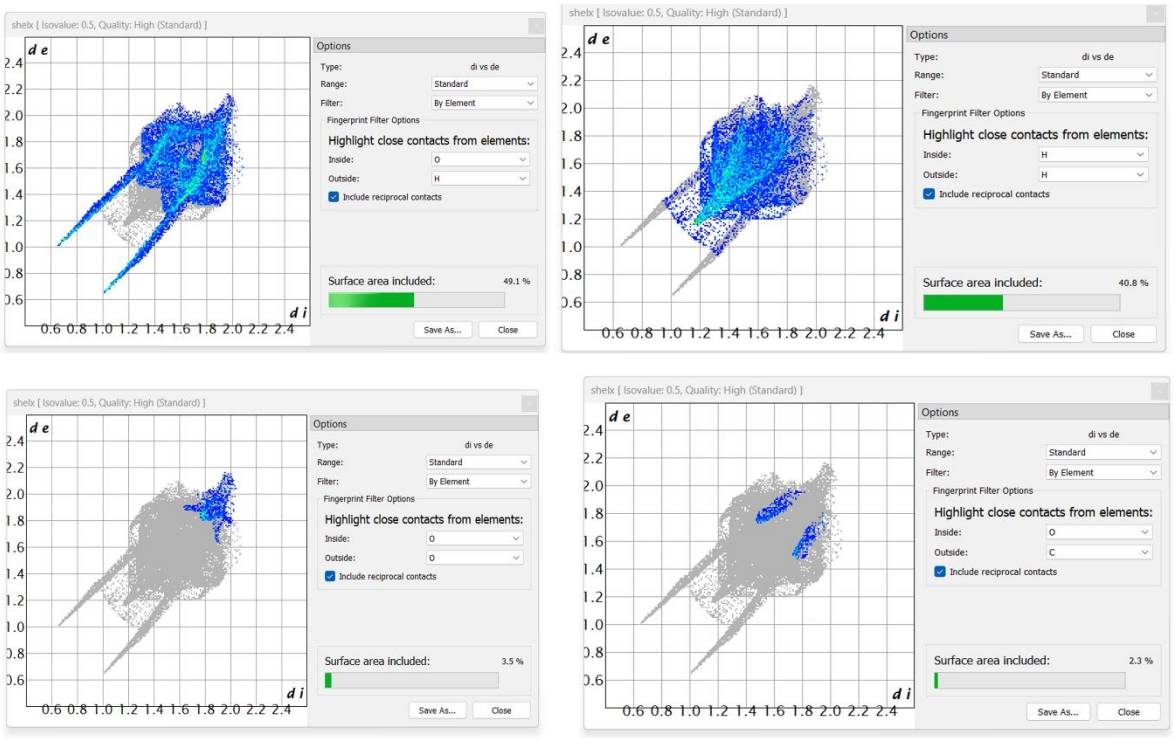

Figure 12. Fingerprint plot of adipic acid molecule

4.8 Hirshfeld surface (HS) Analysis

Hirshfeld surface calculations and fingerprint graphs investigated the intermolecular contacts inside the researched molecule's crystal structure [45]. The intermolecular forces that influence the creation of different supramolecular arrangements in the framework of crystals can only be compared with these

investigations[46]. Contributor and receiver atoms with substantial intermolecular hydrogen bonding are indicated as red patches on the HS, depicted with the d_{norm} variable (-0.7295 to 1.0024 Å) (Figure 11). The d_{norm} parameter, which reflects the normalized collision distance, is utilized in O···H-C/C-H···O interactions. This disparity is computed using two formulas: di, which is the distance (Figure 11) from a nucleus within the HS to a certain point on the surface, and de, which is the distance (Figure 11) from a nucleus beyond the HS to a similar place on the surface [47,48]. The curvature & shape index of the HS (Figure 11) show C-H…π and π-π stacking relationships represented by neighboring red and blue triangles (Figure 11). It is evident that there are no π–π interactions when there are no such adjacent triangles. Several noteworthy intermolecular interactions revealed by HS analysis are depicted together in Figure 11. Short contacts are identified by adding the lengths of the two surfaces, de and di, which result in the following values: 1.672 Å, 3.612 Å, 3.426 Å, and 2.161 Å. These separations are indicative of strong ties. Further information about the intermolecular contacts may be gained from the 2-D fingerprint charts, which indicate that the compound's most common affinities are reciprocal O···H/H···O, H···H, O···C/C···O, and O ···O, with consecutive values of 49.1%, 40.8%, 23.2%, and 3.5% (figure 12).

5. Conclusion

Using a variety of scientific methods, this study provides a thorough analysis of the compound ADPI in order to reveal its characteristics and actions. Deeper understanding of different structural characteristics was made possible by determining the single-crystal structure. All required input files for theoretical calculations were then prepared and successfully carried out, yielding satisfying findings. From optimized geometry the carboxylic group in ADPI significantly influences bond lengths and angles, with theoretical and experimental values closely aligning, revealing strong effects of electronegative oxygen on molecular geometry and electron distribution. The vibrational movements, chemical structure, and bonding interactions of ADPI were better understood using vibrational spectrum analysis. According to FT-IR spectra and theoretical values with high PED accuracy, this study demonstrates that the carboxylic (-COOH) group in ADPI actively participates in hydrogen bonding networks, which have a significant impact on the vibrational frequencies of O-H and C=O groups. Hydrogen bonding interactions consistently lower the O-H stretching frequencies and affect CH_2 vibrations due to intramolecular C-H...O contacts. A high electrophilicity index (ω) and a noteworthy HOMO-LUMO energy gap of 3.6174 eV, which indicate significant charge transfer potential and robust chemical stability, especially within the carboxylic acid group, are two indicators of ADPI 's strong electrophilic behavior, according to the study. Using RDG analysis, the study shows that ADPI has moderate noncovalent interactions, such as C-H···O hydrogen bonding. The study indicates that during CV analysis, ADPI exhibits increasing specific capacitance with increasing scan rates, indicating improved ion diffusion efficiency and charge storage properties that are advantageous for its use in electrochemical energy storage devices. The impedance analysis of ADPI reveals low charge transfer resistance and effective ion diffusion, key traits that support its suitability for high-performance electrochemical applications such as supercapacitors, where rapid charge-discharge cycles are crucial.

References

[1] H. Li, Y. Yu, T. Wang, Y. Zhang, J. You, F. Hu, K. Zhu, Zinc-ion hybrid capacitors: Electrode material design and electrochemical storage mechanism. Journal of Power Sources, 610, (2024) 234638. https://doi.org/10.1016/j.jpowsour.2024.234638

[2] X. Xia, X. Zhang, S. Yi, H. Chen, H. Liu, Supercapacitance properties of porous carbon from chemical blending of phenolic resin and aliphatic dicarboxylic acids. Journal of Materials Research, 31, (2016) 1665–1673. https://doi.org/10.1557/jmr.2016.183

[3] M. Pershaanaa, S. Bashir, S. Ramesh, K. Ramesh, Every bite of Supercap: A brief review on construction and enhancement of supercapacitor. Journal of Energy Storage, 50, (2022) 104599. https://doi.org/10.1016/j.est.2022.104599

[4] T. Chen, L. Dai,s Carbon nanomaterials for high-performance supercapacitors. Materials Today, 16(7), (2013) 272–280. https://doi.org/10.1016/j.mattod.2013.07.002

[5] Y. Wen, X. Wang, H. Wei, B. Li, P. Jin, L. Li, A large-scale continuous-flow process for the production of adipic acid via catalytic oxidation of cyclohexene with H_2O_2. Green Chemistry, 14, (2012) 2868. https://doi.org/10.1039/C2GC35677E

[6] S. Van De Vyver, Y. Román-Leshkov, Emerging catalytic processes for the production of adipic acid. Catalysis Science & Technology, 3, (2013) 1465–1479. https://doi.org/10.1039/C3CY20728E

[7] L. Adili, L. Roufegarinejad, M. Tabibiazar, H. Hamishehkar, A. Alizadeh, Development and characterization of reinforced ethyl cellulose based oleogel with adipic acid: Its application in cake and beef burger. LWT, 126, (2020)

109277. https://doi.org/10.1016/j.lwt.2020.109277

[8] K. Vibha, S. Negi, Enzymatic plasticising of lignin and styrene with adipic acid to synthesize a biopolymer with high antioxidant and thermostability. Polymer Degradation and Stability, 174, (2020) 109081. https://doi.org/10.1016/j.polymdegradstab.2020.109081

[9] G. Lesage, I. Quesada Peñate, P. Cognet, M. Poux, Green Process for Adipic Acid Synthesis: Oxidation by Hydrogen Peroxide in Water Micromelusions using Benzalkonium Chloride C12-14 Surfactant. International Journal of Chemical Reactor Engineering, 10(1), (2012). https://doi.org/10.1515/1542-6580.2955

[10] J. Alcañiz-Monge, G. Trautwein, A. Garcia-Garcia, Influence of peroxometallic intermediaries present on polyoxometalates nanoparticles surface on the adipic acid synthesis. Journal of Molecular Catalysis A: Chemical, 394, (2014) 211–216. https://doi.org/10.1016/j.molcata.2014.07.023

[11] S.T. Gunday, E. Cevik, A. Yusuf, A. Bozkurt, Nanocomposites composed of sulfonated polysulfone/hexagonal boron nitride/ionic liquid for supercapacitor applications. Journal of Energy Storage, 21, (2019) 672–679. https://doi.org/10.1016/j.est.2019.01.008

[12] L. Boonen, P. Kitzler, J. Kasum, Processing of aqueous polymer electrolytes for supercapacitors via different industrial application methods. Progress in Organic Coatings, 115, (2018) 107–114. https://doi.org/10.1016/j.porgcoat.2017.10.006

[13] A. Mazzi, S. Paul, F. Cavani, R. Wojcieszak, Cyclohexane Oxidation to Adipic Acid Under Green Conditions: A Scalable and Sustainable Process. Chemical Catalysis Chemistry, 10(17), (2018) 3680–3682. https://doi.org/10.1002/cctc.201800419

[14] S. Bibi, E. Pervaiz, M. Yang, O. Rabi, Mof embedded and cu doped ceo2 nanostructures as efficient catalyst for adipic acid production: Green catalysis. Catalysts, 11(3), (2021) 304. https://doi.org/10.3390/catal11030304

[15] S. Rajkumar, S. Dhineshkumar, N. Arunprakash, P. Raychel, S. Anantha kumar, J.P. Merlin, Fabrication of $SrWO_4$/PPy composite as electrode material for high-performance supercapacitors. Optical Materials, 142, (2023) 113934. https://doi.org/10.1016/j.optmat.2023.113934

[16] A.A.J. Ranchani, V.S.J. Reeda, P. Divya, R. Suja, V.B. Jothy, Leveraging the properties of pyridine derivatives using DFT analysis to achieve breakthroughs in supercapacitance advancements. Ionics, 30, (2024) 6451–6473. https://doi.org/10.1007/s11581-024-05736-6

[17] M.J. Frisch, G.W. Trucks, H.B. Schlegel, G.E. Scuseria, M.A. Robb, J.R. Cheeseman, G. Scalmani, V. Barone, B. Mennucci, G.A. Petersson, H. Nakatsuji, M. Caricato, X. Li, H.P. Hratchian, A.F. Izmaylov, J. Bloino, G. Zheng, J.L. Sonnenberg, M. Hada, M. Ehara, K. Toyot, R. Fukuda, J. Hasegawa, M. Ishida, T. Nakajima, Y. Honda, O. Kitao, H. Nakai, T. Vreven, J.A. Montgomery Jr., J.E. Peralta, F. Ogliaro, M. Bearpark, J.J. Heyd, E. Brothers, K.N. Kudin, V.N. Staroverov, R. Kobayashi, J. Normand, K. Raghavachari, A. Rendell, J.C. Burant, S.S. Iyengar, J. Tomasi, M. Cossi, N. Rega, J.M. Millam, M. Klene, J.E. Knox, J.B. Cross, V. Bakken, C. Adamo, J. Jaramillo, R. Gomperts, R.E. Stratmann, O. Yazyev, A.J. Austin, R. Cammi, C. Pomelli, J.W. Ochterski, R.L. Martin, K. Morokuma, V.G. Zakrzewski, G.A. Voth, P. Salvador, J.J. Dannenberg, S. Dapprich, A.D. Daniels, O. Farkas, J.B. Foresman, J.V. Ortiz, J. Cioslowski, D.J. Fox, (2010) Gaussian 09, Revision B.01. Gaussian Inc., Wallingford.

[18] M.H. Jamróz, Vibrational energy distribution analysis (VEDA): scopes and limitations. Spectrochimica Acta Part A: Molecular and Biomolecular Spectroscopy, 114, (2013) 220-230. https://doi.org/10.1016/j.saa.2013.05.096

[19] K.R. Dennington, T.A. Keith, J.M. Millam, Semichem, Inc, Shawnee mission, Gaussview, 2019.

[20] T. Lu, F. Chen, Multiwfn: A multifunctional wavefunction analyzer. Journal of Computational Chemistry, 33(5), (2012) 580–592. https://doi.org/10.1002/jcc.22885

[21] H. William, VMD-visual molecular dynamics. Journal of molecular graphics, 14, (1996) 33-38. https://doi.org/10.18974/tvrsj.10.2_231

[22] T. Ben Issa, F. Sayari, H. Ghalla, L. Benhamada, Synthesis, crystal structure, DFT calculations and molecular docking of L-pyroglutamic acid. Journal of Molecular Structure, 1178, (2019) 436–449. https://doi.org/10.1016/j.molstruc.2018.10.033

[23] N.P. Roeges, J.M.A. Baas, (1994) A guide to the complete interpretation of infrared spectra of organic structures. Wiley, New York.

[24] P. Divya, V.S. Jeba Reeda, R. Suja, V. Bena Jothy, Structural activity, spectroscopic, Fukui, NCI, AIM, IGM combined with molecular docking and molecular dynamics simulation on 4-methylpyridinium 4-hydroxybenzoate-potent drug anti-leukemia cancer. Spectrochimica Acta Part A: Molecular and Biomolecular Spectroscopy, 306, (2024) 123568. https://doi.org/10.1016/j.saa.2023.123568

[25] A. Ram Kumar, C. Senthamil Selvi, S. Selvaraj, G.P. Sheeja Mol, P. Jayaprakash, In silico studies on the molecular geometry, FMO, mulliken charges, MESP, ADME and molecular docking prediction of pyrogallol carboxaldehydes as potential anti-tumour agents, Physical Chemistry Research 12 (2) (2024) 305-320, https://doi.org/10.22036/PCR.2023.402835.2359

[26] P. Divya, V.S.J. Reeda, S. Renuga, C.D. Annapoorani, V.B. Jothy, Vibrational analysis, DFT computations of spectroscopic, non-covalent analysis with molecular docking and dynamic simulation of 2-amino-4, 6-dimethyl pyrimidine benzoic acid. Journal of Molecular Structure, 1318, (2024) 139160. https://doi.org/10.1016/j.molstruc.2024.139160

[27] G.S. Fasiuddin, F. Liakath Ali Khan, S. Sakthivel, S. Muthu, A. Irfan, Synthesis, Spectroscopic, Molecular Docking and inhibitory activity of 6-Bromo-2-(4-chlorophenyl)-1H-benzimidazole- a DFT approach. Journal of Molecular Structure, 1261, (2022) 132815. https://doi.org/10.1016/j.molstruc.2022.132815

[28] V.J. Reeda, S. Sakthivel, P. Divya, S. Javed, V.B. Jothy, Conformational stability, quantum computational (DFT), vibrational, electronic and non-covalent interactions (QTAIM, RDG and IGM) of antibacterial compound N-(1-naphthyl)ethylenediamine dihydrochloride. Journal of Molecular Structure, 1298, (2024) 137043. https://doi.org/10.1016/j.molstruc.2023.137043

[29] K. Thirunavukkarasu, P. Rajkumar, S. Selvaraj, S. Gunasekaran, S. Kumaresan, Electronic structure, vibrational (FT-IR and FT-Raman), UV–Vis and NMR analysis of 5-(4-(2-(5-ethylpyridin-2-yl) ethoxy) benzyl) thiazolidine-2,4-dione by quantum chemical method. Chemical Data Collections, 17–18, (2018) 263–275. https://doi.org/10.1016/j.cdc.2018.09.006

[30] P. Divya, V.S. Jeba Reeda, V. Bena Jothy, Fungicide compound 2, 3-dichloronaphthalene-1, 4-dione: Non-covalent interactions (QTAIM, RDG and ELF), combined vibrational spectroscopic investigations using DFT approach with experimental analysis, electronic, molecular docking scrutiny in-vitro assay and thermodynamic property analysis. Journal of Molecular Liquids, 400, (2024) 124544. https://doi.org/10.1016/j.molliq.2024.124544

[31] A. Savin, The electron localization function (ELF) and its relatives : interpretations and difficulties. Journal of Molecular Structure: Theochem, 727(1-3), (2005) 127–131. https://doi.org/10.1016/j.theochem.2005.02.034

[32] A. Ram Kumar, S. Selvaraj, G.P. Sheeja Mol, M. Selvaraj, L. Ilavarasan, S.K. Pandey, P. Jayaprakash, S. Awasthi, O. Albormani, A. Ravi, Synthesis, solvent-solute interactions (polar and non-polar), spectroscopic insights, topological aspects, Fukui functions, molecular docking, ADME, and donor-acceptor investigations of 2-(trifluoromethyl)benzimidazole: A promising candidate for antitumor pharmacotherapy. Journal of Molecular Liquids, 393(1), (2024) 123661. https://doi.org/10.1016/j.molliq.2023.123661

[33] B. Silvi, A. Savin, Classification of chemical bonds based on topological analysis of electron localization functions. Nature, 371, (1994) 683–686. https://doi.org/10.1038/371683a0

[34] V.S. Jeba Reeda, P. Divya, A. Amala Jeya Ranchani, A. Manikandan, S. Alvi, R. Ali, N. Siddiqui, N. Haq, S. Muthu, R. Butcher, S. Javed, Comprehensive analysis of 2,5-dimethyl-1-(naphthalen-1-yl)-1H-pyrrole: X-ray crystal structure, spectral, computational, molecular properties, docking studies, molecular dynamics, and MMPBSA. Journal of Molecular Structure, 1321(3), (2025) 140062. https://doi.org/10.1016/j.molstruc.2024.140062

[35] V.S. Jeba Reeda, J.N. CheerlinMishma, P. Divya, R. Suja, A. Manikandan, M. Shahid, H. Arora, A. Ali, N. Siddiqui, S. Javed, Structural, Fukui, non-covalent analysis, molecular docking, free energy landscapes, and principle component analysis of biological active 1,8-naphthalic anhydride. Spectroscopy Letters, (2024) 1–21. https://doi.org/10.1080/00387010.2024.2401990

[36] H. Jacobsen, Localized-orbital locator (LOL) profiles of chemical bonding. Canadian Journal of Chemistry, 86, (2008) 695–702. https://doi.org/10.1139/v08-052

[37] E.R. Johnson, S. Keinan, P. Mori-Sánchez, J. Contreras-García, A.J. Cohen, W. Yang, Revealing noncovalent interactions. Journal of the American Chemical Society, 132(18), (2010) 6498–6506. https://doi.org/10.1021/ja100936w

[38] P.S. Idante, G.C. Apebende, H. Louis, I. Benjamin, U.J. Undiandeye, I.J. Ikot, Spectroscopic, DFT study, and molecular docking investigation of N-(3-methylcyclohexyl)-2-phenylcyclopropane-1-carbohydrazide as a potential antimicrobial drug. Journal of the Indian Chemical Society, 100(2), (2023) 100806. https://doi.org/10.1016/j.jics.2022.100806

[39] P. Divya, V.S. Jeba Reeda, S. Selvaraj, B. Jothy, Theoretical spectroscopic electronic elucidation with polar and non-polar solvents (IEFPCM model), molecular docking and molecular dynamic studies on bendiocarb - antiallergic drug agent. Journal of Molecular Liquids, 404, (2024) 124895. https://doi.org/10.1016/j.molliq.2024.124895

[40] S. Armaković, S.J. Armaković, Atomistica. online–web application for generating input files for ORCA molecular modelling package made with the Anvil platform. Molecular Simulation, 49(1), (2023) 117-123. https://doi.org/10.1080/08927022.2022.2126865

[41] S. Armaković, S.J. Armaković, Online and desktop graphical user interfaces for xtb programme from atomistica. online platform. Molecular Simulation, 50(7-9), (2024) 560-570. https://doi.org/10.1080/08927022.2024.2329736

[42] T.K. Kuruvilla, S. Muthu, J.C. Prasana, J. George, S. Sevvanthi, Spectroscopic (FT-IR, FT-Raman), quantum mechanical and docking studies on methyl[(3S)-3-(naphthalen-1-yloxy)-3-(thiophen-2-yl)propyl]amine. Journal of Molecular Structure, 1175(5), (2019) 163–174. https://doi.org/10.1016/j.molstruc.2018.07.097

[43] A. Ram Kumar, S. Selvaraj, M. Azam, G. Sheeja Mol, N. Kanagathara, M. Alam, P. Jayaprakash, Spectroscopic, Biological, and Topological Insights on Lemonol as a Potential Anticancer Agent. ACS Omega, 8, (2023) 31548–31566. https://doi.org/10.1021/acsomega.3c04922

[44] S.K. Pathak, R. Srivastava, A.K. Sachan, O. Prasad, L. Sinha, A.M. Asiri, M. Karabacak, Experimental (FT-IR, FT-Raman, UV and NMR) and quantum chemical studies on molecular structure, spectroscopic analysis, NLO, NBO and reactivity descriptors of 3,5-Difluoroaniline. Spectrochimica Acta Part A: Molecular and Biomolecular Spectroscopy, 135, (2015) 283–295. https://doi.org/10.1016/j.saa.2014.06.149

[45] C. Karnan, A. Ram Kumar, S. Selvaraj, Quantum Chemical Computational Studies on the Structural Aspects, Spectroscopic Properties, Hirshfeld Surfaces, Donor-Acceptor Interactions and Molecular Docking of Clascosterone: A Promising Antitumor Agent. International Research Journal of Multidisciplinary Technovation, 6, (2024) 32–53. https://doi.org/10.54392/irjmt2444

[46] A. Ram Kumar, N. Kanagathara, S. Selvaraj, Spectroscopic, Structural and Molecular Docking Studies on N, N-Dimethyl-2-[6-methyl-2-(4-methylphenyl) Imidazo [1, 2-a] pyridin-3-yl] Acetamide, Physical Chemistry Research 12 (1) (2024) 95-107, https://doi.org/10.22036/PCR.2023.387911.2306

[47] P.R. Spackman, M.J. Turner, J.J. McKinnon, S.K. Wolff, D.J. Grimwood, D. Jayatilaka, M.A. Spackman, CrystalExplorer: A program for Hirshfeld surface analysis, visualization and quantitative analysis of molecular crystals. Journal o Applied Crystallography, 54, (2021) 1006–1011. https://doi.org/10.1107/S1600576721002910

[48] Y. Megrouss, Y. Salem, A. Mansour, B. Zohra Douaa, K. Sid Ahmed, H. Benaissi, M. Drissi, Abdelkader, C. (2024). Molecular Structure, Lattice Energy, Hirshfeld Surface and NCI-RDG Analysis, DFT Calculations, and In Silico Molecular Docking of an Imidazole Derivative. Physical Chemistry Research, 12(4), 975-990.

Data Availability

The data supporting the findings of this study can be obtained from the corresponding author upon reasonable request.

Funding

The author declare that no funds, grants or any other support were received during the preparation of this manuscript.

Has this article screened for similarity?

Yes

About the License